Suppressed deprotonation enables a durable buried interface in tin-lead perovskite for all-perovskite tandem solar cells

Sheng Fu[1,6*], Nannan Sun[1,6], Yeming Xian[1,6], Lei Chen[1], You Li[1], Chongwen Li[2], Abasi Abudulimu[1], Prabodika N. Kaluarachchi[1], Zixu Huang[3], Xiaoming Wang[1], Kshitiz Dolia[1], David S. Ginger[3,4], Michael J. Heben[1], Randy J. Ellingson[1], Bin Chen[2], Edward H. Sargent[2,5], Zhaoning Song[1*], Yanfa Yan[1, 7*]

[1]Department of Physics and Astronomy and Wright Center for Photovoltaics Innovation and Commercialization, University of Toledo, Toledo, OH, USA 43606.

[2]Department of Chemistry, Northwestern University, Evanston, Illinois 60208, United States.

[3]Department of Chemistry, University of Washington, Seattle, Washington 98195, United States.

[4]Physical Sciences Division, Physical and Computational Sciences Directorate, Pacific Northwest National Laboratory, Richland, Washington 99352, United States.

[5]Department of Electrical and Computer Engineering, Northwestern University, Evanston, Illinois 60208, United States.

[6]These authors contributed equally to this work.

[7]Lead contact

*Correspondence: sheng.fu2@utoledo.edu, zhaoning.song@utoledo.edu, yanfa.yan@utoledo.edu

SUMMARY

Low-bandgap tin (Sn)-lead (Pb) perovskites are a critical component in all-perovskite tandem solar cells, dictating their efficiency and durability. However, the current state-of-the-art Sn-Pb perovskite solar cells exclusively use poly(3,4-ethylenedioxythiophene)-poly(styrenesulfonate) (PEDOT:PSS) as the hole transport layer (HTL), but suffer from a significant consequence, i.e., it causes undesired buried interface degradation. Here, we show that the deprotonation of the -SO_3H group in PSS is the root cause of the interface degradation due to its low acid dissociation constant (pK_a), which leads to acidic erosion and iodine volatilization in Sn-Pb perovskites under operational conditions. We identify that HTL materials featuring the carboxyl (-COOH) group with a higher pK_a, such as poly[3-(4-carboxybutyl)thiophene-2,5-diyl] (P3CT), can simultaneously suppress the deprotonation and strengthen the interface binding with Sn-Pb perovskite, mitigating the buried-interface degradation. Motivated by established P3CT-X modification, we introduce Pb doping to P3CT to increase its work function and reduce energy loss at the interface. The Pb-doped P3CT HTL enabled us to fabricate efficient and stable all-perovskite tandem solar cells with a champion efficiency of 27.8% and an operational lifetime of over 1,000 h with 97% retaining efficiency under maximum power point tracking.

INTRODUCTION

Owing to the outstanding photoelectrical properties of metal halide perovskites and the tremendous efforts of researchers worldwide, perovskite solar cells (PSCs) have significantly progressed over the past decade.[1-6] The record power conversion efficiency of single-junction PSCs has surpassed 26.1%, approaching the Shockley–Queisser (S-Q) detailed balance efficiency limit.[5,7] To overcome the efficiency limit of single-junction devices, a viable approach is to develop multi-junction tandem solar cells by combining two or more semiconductor absorber layers with complementary bandgaps to simultaneously reduce thermalization loss and widen the collection of the solar spectrum.[8-14] A recent breakthrough in monolithic perovskite-silicon tandem solar cells with a certified efficiency of 33.9% manifested the potential of perovskite tandem photovoltaic (PV) technologies that can eclipse the S-Q limit of single-junction solar cells.[7]

All-perovskite tandem solar cells (APTSCs) consisting of a wide-bandgap (WBG, 1.7 -1.8 eV) top cell with a low-bandgap (LBG, 1.2-1.3 eV) bottom cell offer a unique avenue to realize ultra-high efficiency thin-film tandem devices at low economic and environmental costs.[15-18] They have attracted substantial interest in recent years and rapidly advanced to achieve high certified efficiencies of more than 29%, outperforming their single-junction perovskite counterparts. The progress of APTSCs has been mainly driven by the advances in their key component of the LBG perovskite subcell.[19,20] Many efforts have been devoted to improving film quality and reducing undesired non-radiative recombination in LBG PSCs, such as crystallization

controls,[15,21-24] defects passivation,[5,25-27] and functional surface layer construction[10]. Despite impressive improvements in efficiency, the durability of both LBG and APTSCs still lagged far behind their single-junction Pb-perovskite counterparts due to the ease of degradation in the Sn-containing LBG perovskites.[28,29]

Currently, almost all high-efficiency APTSCs use poly(3,4ethylenedioxythiophene)-poly(styrenesulfonate) (PEDOT:PSS) as the hole transfer layer (HTL) (**Table S1**). However, PEDOT:PSS with the sulfonate group (-SO_3H) causes degradation of halide perovskites due to its hygroscopic and strongly acidic properties.[30-33] Particularly, it triggers iodide redox reactions ($2I^- \rightarrow I_2$) and tin oxidation ($Sn^{2+} \rightarrow Sn^{4+}$) at its interface with Sn-Pb perovskites. These redox reactions create a large number of iodine vacancies (V_I) and tin vacancies (V_{Sn}), hindering charge carrier extraction and increasing non-radiative recombination. Moreover, the adverse interfacial reactions are exacerbated under stressed conditions,[33,34] severely worsening the stability of LBG PSCs and APTSCs. Although mitigation strategies have been explored to alleviate the detrimental interface degradation,[31,32,35-37] the ubiquitous use of PEDOT:PSS in the LBG subcell remains a major stability challenge for high-efficiency APTSCs. A comprehensive understanding of the interface reactions between PEDOT:PSS and Sn-Pb perovskite has yet to be addressed, and more effective strategies are needed to develop desirable HTLs for stable and efficient APTSCs.

In this work, we identify that the deprotonation of PSS is the primary cause of the photoinduced interface degradation of Sn-Pb perovskite solar cells. Our density-functional theory (DFT) calculation shows that the deprotonation of the -SO_3H group

in PSS significantly lowers the energy barrier for the formation of iodine vacancy (V_I) at the perovskite/HTL interface and releases volatile hydrogen iodide (HI). We show that electron delocalization in the benzene-SO_3^- radical significantly weakens the bond of O-H, resulting in the low acid dissociation constant (pK_a) of PSS. We further show that alternative HTLs with -COOH, such as poly[3-(4-carboxylatebutyl)thiophene (P3CT), display less electron delocalization, providing an effective strategy to suppress the deprotonation from the HTL. Motivated by previous works on P3CT-X modification (X = methylamine or alkali metal cations) that have been used in a variety of PSCs,[38-41] we introduce Pb-doping to increase its work function and minimize the energy level offset with the Sn-Pb perovskite. The Pb dopants also provide nucleation sites to enable high-quality Sn-Pb perovskite film growth. Therefore, replacing the traditional PEDOT:PSS HTL with Pb-doped P3CT enabled us to fabricate efficient LBG PSCs and APTSCs with improved stability. We demonstrated LBG PSCs and APTSCs with champion efficiencies of 22.7% and 27.8%. Importantly, an APTSC retained >90% of its initial efficiency after maximum power point tracking under nearly 1 sun illumination for over 1000 h.

RESULTS AND DISCUSSION

Theoretical calculations on the perovskite/HTL interface and molecular design

Acidic functional groups are commonly included in the organic HTL of PSCs to form strong bonds with both the transparent conducting oxide (TCO) on the substrate and perovskite layer, promoting uniform perovskite film deposition over a large

area.[42,43] However, acid dissociation from HTLs may introduce a severe challenge to the durability of PSCs. Notably, the stability of most high-efficiency Sn-containing PSCs and APTSCs is seriously limited by the -SO_3H group in PEDOT:PSS, owing to the inevitable surface reactions. We performed DFT calculations of the $APb_{0.5}Sn_{0.5}I_3$/PSS (A = methylammonium and formamidinium, or MA and FA) interface to identify the degradation mechanism of acidity-induced interface degradation. As shown in **Figure 1A**, a PSS molecule binds to the $MAPb_{0.5}Sn_{0.5}I_3$ perovskite surface with the Pb(Sn)-I termination and releases a proton (H^+), which then extracts an I atom from the perovskite surface, forming an I vacancy (V_I) at the perovskite interface and HI as a decomposition byproduct. This process facilitates the subsequent escape of HI and MA gas molecules, which is energetically more favorable by 0.19 eV as compared to the escape of HI and MA molecules on the bare perovskite surface without the influence of PSS (**Figure S1**). The released I may also form I_2 and oxidize the Sn^{2+} into Sn^{4+}, inducing catastrophic interface degradation. Similar DFT calculations were carried out on the MA-I terminated surface (**Figure S2**) and on $FAPb_{0.5}Sn_{0.5}I_3$ perovskite (**Figure S3**), showing reduced formation energy for organic and HI gas species after binding a PSS molecule on the perovskite surface. This acidic reaction at the perovskite/HTL interface is likely to cause buried interface degradation in LBG PSCs and APTSCs.

To better understand the acidic dissociation from PSS, we calculated the charge distribution in the basic carboxylic, phosphonate, and sulfonate groups. **Figure 1B** presents the Hirshfeld charge distribution in representative molecules with the simplest

structures. Their relative acidity, defined as the capability to donate a proton and form a conjugate base, can be evaluated by the negative charge located on the oxygen atom bonded with the hydrogen. The calculated charge distributions on the O of the -OH in carboxylic (-COOH), phosphonate (-PO_3H_2), and sulfonate (-SO_3H) moieties attached with a methyl group are -0.672, -0.626, and -0.579, respectively. A more negative charge located on the O of -OH indicates a stronger O-H bond and a more polarized (less stable) conjugate base, corresponding to a lower acidity. Therefore, among these acidic groups, -COOH shows the lowest acidity and -SO_3H the highest acidity. The higher acidity of -SO_3H than -PO_3H_2 can be attributed to the higher electronegative of S than P (2.58 eV vs 2.19 eV). With the same coordination, the S atom is expected to accept more negative charge than the P atom due to its higher electronegativity, resulting in less electron charge on the O atom of the -OH group in -SO_3H, making it easier to lose the proton. To quantify the deprotonation properties of different acidic functional groups, we calculated the acid dissociation constant (pK_a) for these functional groups **(Figure 1C)**. The sulfonate group shows the strongest acidity with a pK_a of -1.61, while phosphonate and carboxylic groups show less acidity with pK_a values of 1.87 and 4.54, respectively. The DFT calculations further reveal that the deprotonation energy of CH_3-COOH is 1.13 and 0.66 eV higher than that CH_3-SO_3H and CH_3-PO_3H_2, respectively. Therefore, the close-to-neutral (high pK_a) functional group based on -COOH can potentially ameliorate interface degradation at the Sn-Pb perovskite/HTL interface.

Figure 1D shows the molecular structure and pK_a of three commonly used HTLs.

The PSS presents an even lower pK_a (-2.36) than CH_3-SO_3H, which is attributed to the increased electron delocalization of the benzene-SO_3 moiety in its conjugate base. In comparison, the widely used phosphonate acid carbazole (PACz)-based self-assembled monolayer HTL, such as 2PACz, shows a positive pK_a of 1.49, but it is a medium-strong acidity (pK_a<2). Therefore, it may still present a long-term stability challenge if the -PO_3H_2 ends are not entirely bound to the substrate. In contrast, P3CT with a carboxylic group shows a pK_a value as high as 5.23. We found that the P3CT solution shows a close to neutral nature (pH 6-7, **Figure S4**), which is expected to significantly suppress the interface decomposition for efficient and stable Sn-Pb PSCs and ATPSCs.

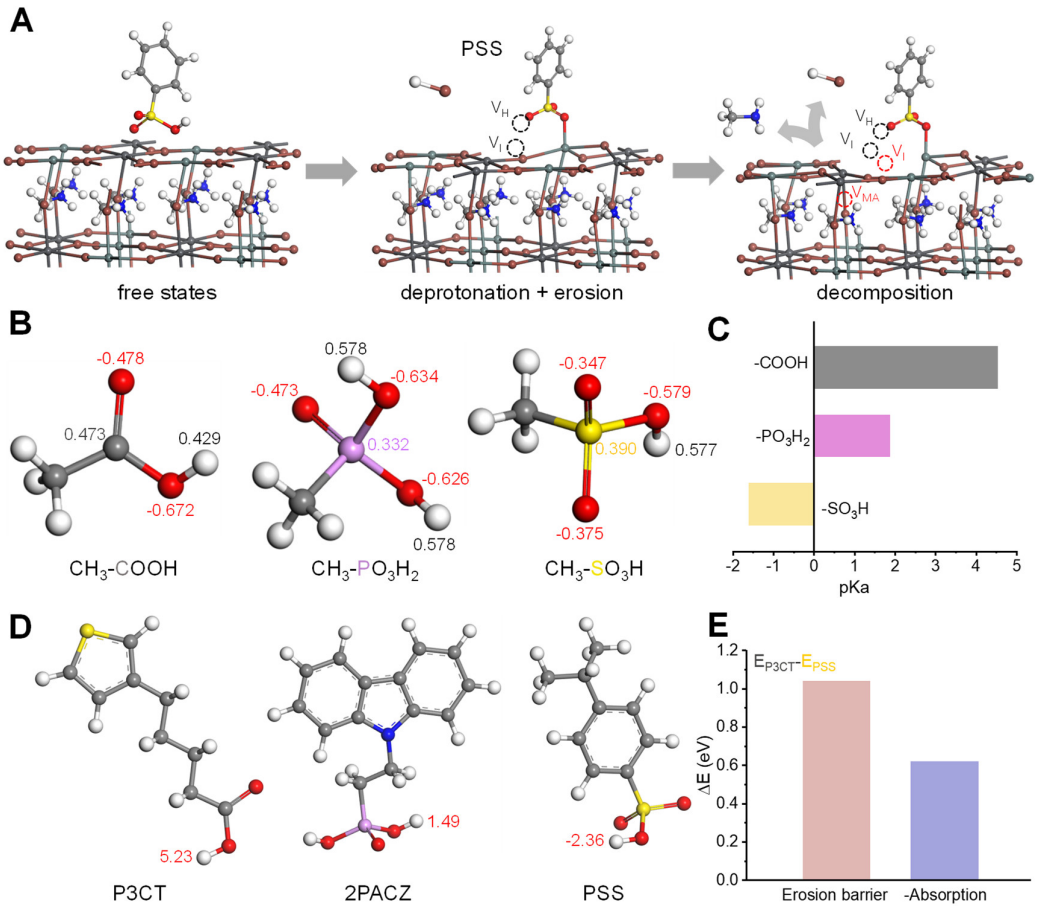

Figure 1. Theoretical calculations on interfacial reaction and molecular designs.

(A) DFT simulations of the reaction and decomposition at the Sn-Pb perovskite/PEDOT:PSS interface.
(B-C) Hirshfeld charge distributions (B) and the calculated pK_a (C) of the carboxylic, phosphonate, and sulfonate functional groups attached to the methyl end.
(D) Molecular structures and pK_a numbers (red) of the reported HTLs for high-efficiency PSCs.
(E) Energy difference (E_{P3CT}-E_{PSS}) of the surface bonding energy and the energy barriers of acidic erosion.

We then calculated formation energy barriers for the deprotonation-erosion process on the Sn-Pb perovskite surface with P3CT and PSS molecules, and their energy differences are presented in **Figure 1E** (detailed diagram of simulations is shown in **Figure S5**). Compared with PSS, P3CT increases the energy barrier of acidic reaction on the perovskite by 1.04 eV, greatly hindering the undesirable acidic erosions at the buried interface. Additionally, P3CT also shows a higher binding strength on the perovskite than the PSS, with an energy difference ΔE_b of 0.62 eV (**Figure S6**), which prevents surface defect formation and inhibits the decomposition of perovskite. Furthermore, we found that the energy barrier for the volitation of MA and HI from perovskite after deprotonation/erosion is increased by 0.1 eV after replacing PSS with P3CT (**Figure S7)**. The calculations reveal that P3CT can suppress acidic erosion and increase bonding energy to the perovskite, promising superior efficiency and stability in ATPSCs.

Stability of the perovskite/HTL interface

To identify the interface reaction at the HTL/Sn-Pb perovskite interface, time-resolved mass spectrometry (TR-MS) measurements were taken under 1 sun illumination incident on the glass side (schematic diagram shown in the inset of **Figure**

2A). **Figure 2A** plots TR-MS evolution traces of HI and MA signals after turning on the illumination. A substantial spike of MA partial vapor pressure accompanied by gradually increasing HI vapor pressure was detected after exposing the Sn-Pb perovskite/PEDOT:PSS sample to 1-sun irradiation. The observed gas signals manifest severe photodegradation at the perovskite/PEDOT:PSS interface. In contrast, the P3CT-Pb/perovskite sample shows much lower vapor pressure of MA and almost negligible HI partial pressure, indicating significantly suppressed surface photodegradation. Additionally, we compared the photodecomposition of Sn-Pb perovskite/HTL interfaces based on MeO-2PACz and neutral HTLs, such as poly(triaryl amine) (PTAA) and PEDOT without PSS (**Figure S8**). The perovskite/MeO-2PACz interface exhibits photodecomposition with MA and HI emissions similar to acidic PEDOT:PSS, which is likely due to the relatively strong acidity of MeO-2PACz (pKa = 1.49). In comparison, PTAA and neutral PEDOT exhibit superior photostability than acidic HTLs. The results agree with the DFT calculations that suppressing the deprotonation of HTLs is significant in prolonging the photostability of Sn-Pb PSCs. Compared with PEDOT (without PSS) and PTAA, P3CT is more suitable for Sn-Pb perovskite and tandem device fabrication owing to its better wettability (**Figure S9**) and effective buried surface passivation.

Figure 2B and **C** compares the SEM images of the buried (bottom) surface of perovskite films before and after light-thermal aging, peeled off from the PEDOT:PSS and P3CT-Pb HTLs, respectively. The fresh perovskite film peeled off from P3CT-Pb shows fewer pores and voids than PEDOT:PSS, benefiting from the stronger interface

binding between perovskite and P3CT-Pb than PEDOT:PSS. After light-thermal aging at 60 °C and 0.9 sun illumination for 5 days, the perovskite film on PEDOT:PSS experienced severe decomposition, creating a large number of voids and microcracks around grain boundaries on the surface (**Figure 2B**) and throughout the perovskite layer (**Figure S10A**). In sharp contrast, the surface and cross-sectional SEM view of the perovskite film on P3CT-Pb remain unchanged after aging under the same conditions (**Figure 2C** and **Figure S10B**), proving its superior stability enabled by a robust interface. To identify the chemical decomposition, we peeled off the perovskite films and soaked them into a toluene solution for light-thermal aging tests. As shown in the inset image of **Figure 2C**, the solution containing the PEDOT:PSS sample became pink after aging for 3 days, while the P3CT-Pb sample remained colorless. The pronounced absorbance peaks associated with I_2 and SnI_4 species appeared in the optical absorbance spectrum of the aged PEDOT:PSS sample but not the P3CT-Pb one (**Figure 2D**), confirming the interface robustness of the P3CT-Pb sample.

We conducted XPS measurements to identify the chemical variations on the buried surface of the perovskite films before and after aging. The pristine Sn-Pb perovskite film deposited on PEDOT:PSS shows remarkably high Sn^{4+} (**Figure 2E** top) and I_0 signals (**Figure S11A**), likely due to the defective interface formation during annealing. The ratios of Sn^{4+}/Sn^{2+} (**Figure 2F** top) and I_0/I (**Figure 2G** top) were significantly increased after light-thermal aging for 5 days, revealing the unstable nature of the perovskite/PEDOT:PSS interface. In contrast, the undesired Sn^{4+} and I_0 signals were suppressed in the fresh perovskite film deposited on the P3CT-Pb HTL (**Figure 2E**

bottom and **Figure S11B**) and were only slightly increased after aging (**Figure 2G**). Additionally, we observed evidence of residue PEDOT:PSS and P3CT on the peeled-off perovskite surface through S-*2p* XPS measurements (**Figure S11C**). After light-thermal aging, the S-*2p* signal in the PEDOT:PSS sample diminished, while that in the P3CT-Pb sample retained (**Figure S11D**), indicating the stronger binding strength for the perovskite/P3CT-Pb interface. These results confirm that the P3CT-Pb HTL can mitigate the buried interface degradation of Sn-Pb perovskites, making it a good candidate for stable LBG PSCs and APTSCs.

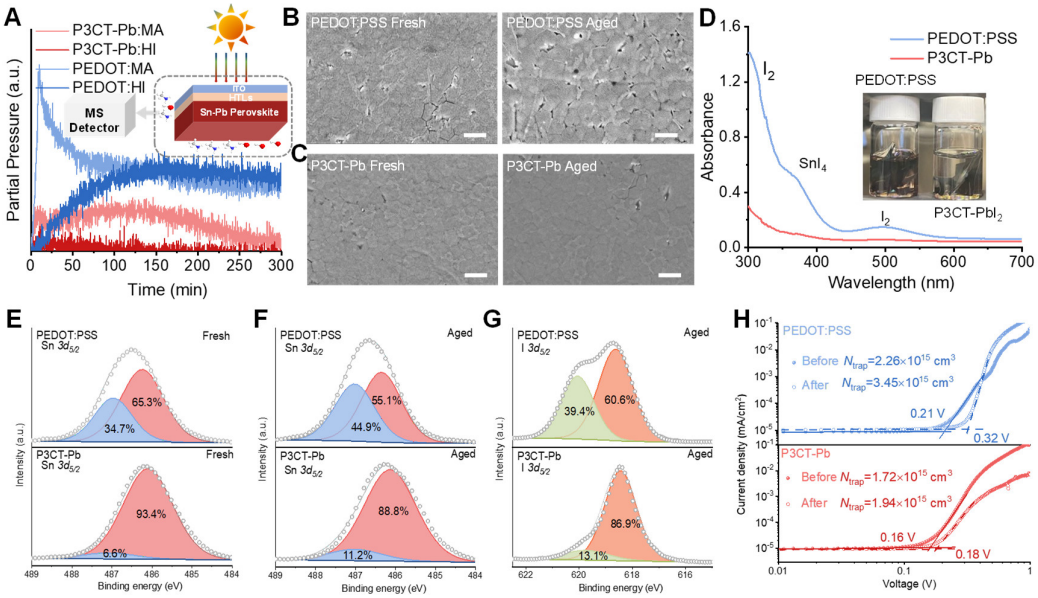

Figure 2. Stability of buried interface with PEDOT:PSS and P3CT-Pb HTLs.
(A) TR-MS results of MA and HI gases releases of Sn-Pb perovskite on PEDOT and P3CT-Pb HTLs. The inset is the schematic diagram of TR-MS measurements.
(B-C) SEM images of the buried surface of Sn-Pb perovskite on PEDOT:PSS (B) and P3CT-Pb (C) before (left) and after (right) aging at 60 ˚C and 0.9 sun illumination (from glass side) for 5 days. The scale bar is 1 μm.
(D) UV-vis absorptance spectra of the toluene solution with the Sn-Pb perovskite films after aging for 3 days. The inset image is a photo of the solutions.
(E-G) Sn 3d XPS spectra of the buried bottom surface of fresh (E) perovskite, Sn 3d XPS spectra (F) and I 3d (G) of aged films on PEDOT:PSS (top) and P3CT-Pb (bottom).
(H) SCLC plots of the perovskite films based on a hole-only device structure.

The trap density (N_t) of the fresh and aged Sn-Pb perovskite films was measured using the space charge limited current (SCLC) method with a hole-only device structure, and the results are presented in **Figure 2H**. Benefiting from stronger interface binding and enhanced crystallinity, the fresh Sn-Pb perovskite film deposited on P3CT-Pb shows a lower N_t of 1.72×10^{15} cm^{-3} than on PEDOT:PSS (2.26×10^{15} cm^{-3}). The N_t of the aged Sn-Pb perovskite film on PEDOT:PSS increased to 3.45×10^{15} cm^{-3}, while the N_t of the aged perovskite on P3CT-Pb only slightly increased to 1.94×10^{15} cm^{-3}. The result confirms that replacing PEDOT:PSS with P3CT-Pb reduces defect density and improves the stability of Sn-Pb perovskite films.

Characterization of perovskite films and LBG PSCs

P3CT has been used as the HTL for a variety of PSCs with remarkable efficiency and stability.[19,38-41,44] However, compared to the more widely used HTLs, such as poly(triaryl amine) (PTAA) and self-assembled monolayers (SAMs),[45-48] the efficiency of P3CT-based PSCs is still limited by a high V_{OC} deficit due to a large valence band mismatch between the P3CT HTL and perovskite. Motivated by the reports in the literatures,[49,50] we considered P3CT doped with metal cations to tune the work function of P3CT. We first prepared P3CT HTLs with different dopants, including methylamine (MA), cesium hydroxide (CsOH), and PbI_2. We evaluated their impact on tuning E_f using Kelvin probe force microscopy (KPFM) measurements (**Figure S12**). P3CT-Pb shows a higher surface work function than P3CT-MA and P3CT-Cs. Additionally, the DFT results (**Figure S13** and **Table S2**) reveal that the Pb doping in P3CT significantly

reduces the positive charges on the Pb cation and increases charge numbers on the S and C atoms of the thiophene ring of the P3CT monomer, indicating that PbI_2 interacts with P3CT by attracting the lone-pair electrons of the S atom on the thiophene ring toward the Pb atom. As shown in **Figure 3A**, obviously higher binding energies of the S-2p orbital levels of thiophene and the reversed shifts of Pb-4f levels (**Figure S14**) are observed when mixing P3CT and PbI_2. This charge transfer increases the hole density in the thiophene chains and down-shifts the Fermi energy (E_f) of the P3CT HTL, which minimizes the band offset between the HTL and perovskite and facilitates hole extraction.

The ultraviolet photoelectron spectroscopy (UPS) spectra of PEDOT:PSS and P3CT were collected (**Figure S15**), and the corresponding energy level diagrams are plotted in **Figure 3B**. The bare P3CT film shows a similar valence band energy level (E_v) but a slightly deeper E_f at -5.08 eV than PEDOT: PSS. After conjugating with PbI_2, the P3CT-Pb film exhibits more negative E_f and E_v levels at -5.13 and -5.36 eV, reducing the E_v offset with the Sn-Pb perovskite. We evaluated the effect of PbI_2 conjugation on the hole conductivity of P3CT using a hole-only structure. The P3CT-Pb film exhibits a higher conductivity than the bare P3CT (**Figure S16**).

We further compared the optical and morphological properties of P3CT and PEDOT: PSS. Despite above-bandgap (~1.9 eV) absorption at short wavelengths, P3CT-Pb shows a higher transmittance at long wavelengths (> 640 nm) than PEDOT: PSS (**Figure S17**), which makes P3CT more desirable for the HTL of the bottom subcell in a tandem structure. Atomic force microscope (AFM) measurements reveal a slightly

higher surface roughness (1.89 nm) for P3CT-Pb than PEDOT: PSS (1.38 nm) (**Figure S18**). The larger roughness with PbI_2 frameworks can act as nucleation seeds to allow the heterogeneous growth of Sn-Pb perovskite films for large grains with improved crystallinity.

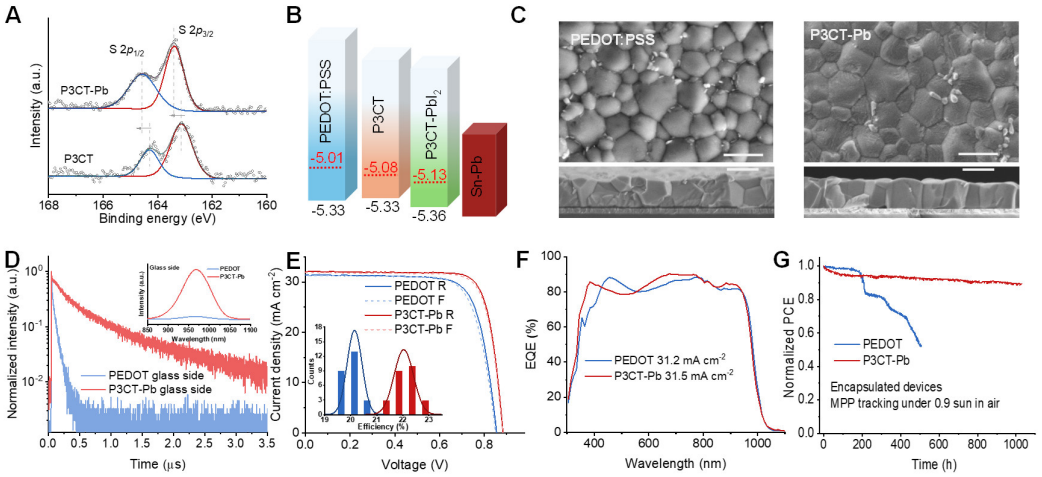

Figure 3. Investigations on the energy level of P3CT-Pb, crystalline and photoelectrical properties and corresponding photovoltaic performance.
(A-B) XPS S 2p level (A) and energy-levels (B) of the P3CT and P3CT-Pb HTLs.
(C) Top-view (top) and cross-section (bottom) SEM images of Sn-Pb perovskite deposited on PEDOT:PSS and P3CT-Pb HTLs. The scale bar is 1 μm.
(D) TRPL and PL curves (inset) of the Sn-Pb perovskite films.
(E-G), J-V curves (E), EQE curves (F) and MPPT stability (G) of the LBG PSCs. The inset in E is the efficiency statistics of the corresponding LBG PSCs.

We further evaluated the crystallinity and structural properties of Sn-Pb films deposited on different HTLs. The scanning electron microscopy (SEM, **Figure 3C**) measurement manifests that Sn-Pb perovskite film deposited on PEDOT: PSS has inhomogeneous surface morphology and relatively small apparent grain domains with an average size of 440 nm (**Figure S19A**). In comparison, the film grown on P3CT-Pb exhibits uniform morphology, featuring larger apparent grain domains with an average size of 670 nm (**Figure S19B**) and crystal terrains on the surface. The cross-sectional

SEM images display more desired columnar grains with larger size for the Sn-Pb perovskite film on P3CT-Pb, well better than the randomly oriented and irregularly shaped grains in the perovskite film on PEDOT: PSS (**Figure 3C**, bottom). Apart from the enhanced microstructures, the perovskite film on P3CT-Pb also shows a smaller surface roughness of 20.5 nm than that on PEDOT: PSS (24.8 nm) (**Figure S20**). A smooth perovskite surface is critical to form good contact with the C_{60} electron-transport layer (ETL) to reduce surface recombination.

We compared the X-ray diffraction (XRD) patterns and optical absorption of the perovskite films. All films present only the α phase of the perovskite with the same characteristic XRD peaks and a bandgap of 1.26 eV (**Figure S21**), indicating the trace amount of PbI_2 from P3CT-Pb has a negligible impact on the perovskite phase and bandgap. The film on P3CT-Pb shows a 2-fold higher XRD intensity and 1.3 times increase in grain size calculated by the Scherrer formula than the film on PEDOT: PSS (**Figure S21A**), which is consistent with the trend of grain size change determined by the SEM measurements. We also assessed the microstructure and crystallinity of perovskite films deposited on different P3CT-based HTLs. The film deposited on P3CT-Pb shows the most intense XRD peaks and the largest grain size among them (**Figure S22**), suggesting the strong interaction between P3CT-Pb and perovskite facilitates the crystallization of Sn-Pb perovskites.

The superior crystallinity of the perovskite on P3CT-Pb also leads to improved photoelectrical properties. The photoexcited charge carrier dynamics of perovskite films deposited on different HTLs were studied by steady-state photoluminescence (PL)

and time-resolved PL (TRPL) measurements. When excited from the film side, the perovskite film on P3CT-Pb presents 100 times higher PL intensity and 18 times higher carrier lifetime than the film on PEDOT:PSS (**Figure S23 and Table S3**), which is attributed to the improved crystallinity and suppressed non-radiative recombination. When excited from the glass (HTL) side (**Figure 3D**), the films present weaker PL peak intensity and shorter TRPL carrier lifetimes due to the fast hole extraction and interface recombination. Apparent improvements in the PL intensity were observed in the perovskite films on P3CT-based HTLs than PEDOT: PSS (**Figure S24**), indicating that P3CT effectively suppresses the undesired non-radiative recombination at the Sn-Pb perovskite/HTL interface. The film on P3CT-Pb shows the highest PL intensity and the longest carrier lifetime among all, revealing its superior defect passivation properties when in contact with the perovskite. We further measured the PL quantum yield (PLQY, **Figure S25**) from the glass side to quantify the quasi-Femi energy splitting in Sn-Pb perovskite films as an impact of interfacial non-radiative recombination. Benefiting from the better energy level alignment and reduced surface defects, the perovskite/P3CT-Pb sample shows the highest PLQY of 2.42%, corresponding to the highest implied V_{OC} of 918 mV.

We fabricated LBG PSCs with the PEDOT:PSS and P3CT HTLs in the device structure of ITO/HTL/Sn-Pb perovskite/C_{60}/BCP/Ag. **Figure 3E** presents the *J-V* curves of the champion LBG devices based on PEDOT:PSS and P3CT-Pb. The detailed PV parameters are listed in **Table 1**. The device based on PEDOT:PSS shows a PCE of 20.4%, with a V_{OC} of 0.856 V, a short-circuit current density (J_{sc}) of 31.4 mA/cm^2, and

a FF of 75.8%. The devices based on P3CT-based HTLs show improvements in all PV parameters (**Figure S26 and Table S4**). The best-performing device based on P3CT-Pb delivers the highest PCE of 22.7% with a high V_{OC} of 0.884 V, a J_{sc} of 32.0 mA/cm^2, and a FF of 80.3%. The J_{sc} of the LBG PSCs was verified by the external quantum efficiency (EQE) measurements (**Figure 3F**). In agreement with the UV-vis transmittance data, the device based on P3CT-Pb shows lower EQEs at short wavelengths (<600 nm) and higher EQEs at long wavelengths (>600 nm) than the PEDOT:PSS device, resulting in an increased integrated J_{SC} from 31.2 to 31.5 mA/cm^2. We fabricated 25 individual devices for each group, and their statistical results are presented in **Table 1** and **Figure S27**. The devices based on PC3T-Pb show remarkable enhancements in V_{OC}, FF, and thus PCE (**Figure 3E inset**), with narrower distribution and better reproducibility than those based on PEDOT:PSS. This improvement is mainly attributed to the perovskite/P3CT-Pb interface, which has stronger interface binding, better energy level alignment, and superior charge carrier extraction properties than the interface with PEDOT:PSS.

Capacity-voltage (*C-V*) measurements were conducted to understand the improved device performance of corresponding LBG PSCs. Due to the poor crystallinity and high defect density at the buried interface, the device on PEDOT:PSS suffers from a poor diode quality with a considerable leakage current and a low built-in potential (V_{bi}) of 0.705 V (**Figure S28**). With more desirable energy level alignment and interface passivation, the device with P3CT-Pb shows an increased V_{bi} of 0.758 V and a better diode ideality factor. We also conducted the transient photovoltage (TPV) and

photocurrent (TPC) measurements to study the carrier transport dynamics in LBG PSCs. As presented in **Figure S29A**, the device with the P3CT-Pb HTL shows a slower photovoltage decay than the PEDOT:PSS-based one, indicating reduced non-radiative recombination in the devices. Meanwhile, the TPC curves display a shorter decay in the P3CT-based cells than PEDOT:PSS (**Figure S29B**), indicating fast carrier extraction. Additionally, Nyquist analysis shows that the P3CT-based device has larger recombination resistance and smaller series resistance than the PEDOT:PSS-based one (**Figure S30**).

Table 1| Photovoltaic parameters of the champion efficiency and statistics results of the single LBG and tandem PSCs.

Device structure	HTLs	Scan direction	V_{OC} (V)	J_{sc} (mA cm^{-2})	FF (%)	PCE (%)
Single LBG	PEDOT:PSS	Reverse	0.856	31.4	75.8	20.4
		Forward	0.850	31.3	74.1	19.7
Average			0.849±0.013	31.1±0.5	76.2±1.2	20.2±0.3
Single LBG	P3CT-Pb	Reverse	0.884	32.0	80.3	22.7
		Forward	0.882	31.9	79.5	22.4
Average			0.878±0.005	31.8±0.2	78.8±1.0	22.0±0.4
Tandem	PEDOT:PSS	Reverse	2.096	15.5	81.1	26.4
		Forward	2.096	15.5	79.6	25.9
Average			2.046±0.033	15.4±0.1	79.6±1.1	25.1±0.6
Tandem	P3CT-Pb	Reverse	2.147	15.7	82.6	27.8
		Forward	2.146	15.7	81.5	27.5
Average			2.127±0.017	15.6±0.1	80.9±1.3	27.0±0.6

In addition to improving efficiency, the P3CT-Pb HTL also benefits the thermal

and light stability of Sn-Pb PSCs. A typical cell with the PEDOT:PSS HTL exhibited severe degradation with ~80% efficiency loss after 528 h of thermal aging on a 60 ˚C hotplate (**Figure S31A**), mainly due to the acidic erosion at the perovskite/HTL interface.[33,51] A P3CT-based device stressed under the same condition retained ~90% of its initial efficiency, indicating that replacing the PEDOT:PSS HTL with P3CT-Pb significantly enhances the thermal tolerance of LBG PSCs. Additionally, P3CT-based cells also demonstrated decent operational stability under maximum power point tracking (MPPT) conditions. As shown in **Figure 3G**, A typical P3CT-based Sn-Pb PSC retained ~90% of its initial efficiency after MPPT for more than 1,000 h (T_{90} lifetime), which was well better than a reference cell based on PEDOT:PSS that degraded by ~50% after 500 h. The suppression of HTL deprotonation also benefits the MPPT stability of normal-bandgap Pb-based PSCs. A PSC based on the P3CT-Pb HTL retained >95% of its initial efficiency after 1000 h of continuous operation at 60 °C in the air, demonstrating robust photostability of the perovskite/P3CT interface.

Photovoltaic performance and stability of tandem devices

We fabricated APTSCs with different HTLs for the LBG subcell to evaluate the impact of HTLs on the tandem device performance. The schematic diagram and cross-sectional SEM image of the tandem device are presented in **Figure 4A** and **Figure S32**. The WBG perovskite top subcells used for tandem fabrication show an average efficiency of 18.7% (**Figure S33**). **Figure 4B** presents the J-V curves of the champion tandem cells based on the P3CT-Pb and PEDOT:PSS HTLs. Their detailed parameters are listed in **Table 1**. The PEDOT:PSS-based tandem shows PCE of 26.4 (25.9)%, V_{OC}

of 2.096 (2.096) V, Jsc of 15.5 (15.5) mA/cm^2, and FF of 81.1 (79.6)%, measured by the reverse (forward) scan. In comparison, the champion P3CT-based tandem shows PCE of 27.8 (27.5)%, V_{OC} of 2.147 (2.146) V, J_{sc} of 15.7 (15.7) mA/cm^2, and FF of 82.6 (81.5)%. The stabilized power output (SPO) efficiencies of the devices based on P3CT-Pb and PEDOT:PSS are 27.6% and 25.8%, respectively (**Figure S34**). **Figure 4C** plots the EQE spectra of the tandem cell based on P3CT-Pb, showing the integrated current density of 15.5 and 15.6 mA/cm^2 for the top and bottom subcells, respectively, which are well matched with the J_{sc} of the tandem.

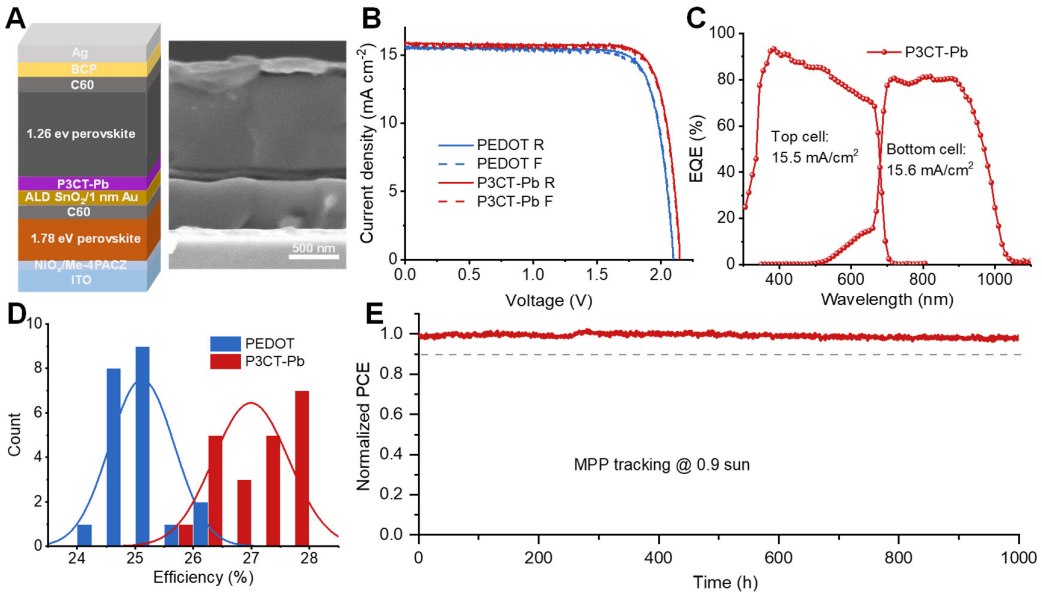

Figure 4. Photovoltaic performance and stability of tandem PSCs.
(A-E) Schematic diagram and cross-section SEM image of the tandem device (A), J-V curves (B), EQE spectra (C), statistic PCE (D), and MPP tracking stability (E) of the tandem PSCs.

The P3CT-based tandems also show a higher average efficiency of 27.0% (**Figure 4D**) with improved V_{OC} and FF (**Figure S35**) than PEDOT:PSS-based devices, proving excellent reproducibility of the high-efficiency tandems with the P3CT-Pb HTL. To

evaluate the tandem stability, we measured the MPPT of the encapsulated tandem cells in air. Impressively, the device remained at 97% of its initial efficiency after continuous tracking for 1000 h (**Figure 4E**), which was substantially improved compared with state-of-the-art APTSCs based on the PEDOT:PSS HTL (**Table S1**). The enhanced tandem stability is mainly attributed to the stabilized buried interface of the perovskite and P3CT-Pb HTL.

Conclusions

We unveiled that the acid dissociation from the PEDOT:PSS HTL is the primary cause for the buried interface degradation in LBG Sn-Pb PSCs through theoretical and experimental studies. The DFT calculation revealed that deprotonation of acidic HTL monomers can facilitate the formation of V_I defects on the perovskite surface and release HI, lowering the energy barriers of the volatilization of MA and I from the perovskite surface. We further identified that reducing electron delocalization in the conjugate base of an HTL monomer can increase its pK_a and suppress the acid dissociation, improving the HTL/perovskite interface stability. Guided by this strategy, we replaced PEDOT:PSS HTL with a nearly neutral HTL based on P3CT to mitigate the buried interface degradation in LBG PSCs. Additionally, doping P3CT with Pb cations reduced the valence band offset with Sn-Pb perovskite and provided nucleation seeds for enhancing perovskite crystallization, resulting in improved film quality. The use of Pb-doped P3CT enabled us to fabricate efficient and stable APTSCs with an efficiency of 27.8% and a T_{90} MPPT lifetime of over 1,000 h. Our molecular design

strategy on stabilizing the perovskite/HTL interface provides a direction for achieving efficient and stable APTSCs.

EXPERIMENTAL PROCEDURES

Resource Availability

Lead Contact

Further information and requests for resources and materials should be directed to and will be fulfilled by the Lead Contact, Yanfa Yan (yanfa.yan@utoledo.edu).

Materials Availability

This study did not generate new unique materials.

Data and Code Availability

This study did not generate or analyze (datasets or code).

Materials

The solvent of N,N-dimethylformamid (DMF, 99.8%), dimethyl sulfoxide (DMSO, 99.9%), deionized water (H_2O), isopropanol (IPA, 99.5%), methanol (Me-OH, 99.5%), anhydrous ethanol (Et-OH, 99%), anisole (99%) and chlorobenzene (CB, 99.9%) were purchased from Sigma Aldrich. Tin (II) iodine (SnI_2, 99.999% for perovskite precursor), tin (II) fluorine (SnF_2, 99%), polyethylenimine (PEIE, 80% ethoxylated solution), methylamine (MA, 33% w/w in Ethanol), cesium hydroxide (CsOH, monohydrate, 99.95%), lead powder (−100 mesh, 99.95%), ethylenediamine (EDA, 99%), Poly(triaryl amine), Poly[bis(4-phenyl)(2,4,6-trimethylphenyl)amine]

(PTAA), PFN-Br and ammonium thiocyanate (NH_4SCN) were ordered from Sigma-Aldrich. The organic halide salts of methylammonium iodide (MAI), formamidinium iodide (FAI) were obtained from Greatcell Solar Company. Bathocuproine (BCP), lead iodine (PbI_2), lead bromine ($PbBr_2$), 1,3-propane-diammonium iodide ($PDAI_2$), cesium iodine (CsI), [4-(3,6-Dimethyl-9H-carbazol-9-yl)butyl]phosphonate acid (Me-4PACz, >99.0%) and MeO-2PACz were bought from TCI company. NiO_x nanoparticles (NPs) powder were offered by Advanced Election Technology Co., Ltd. Poly(3,4-ethylenedioxythiophene) polystyrene sulfonate solution (PEDOT: PSS) was obtained from Ossila. C60 powder was purchased from Nano-C. ALD precursor of tetrakis(dimethylamino) tin (iv) (99.99%-Sn, 50-1815 Tin) was bought from Strem Chemicals. Poly[3-(4-carboxylbutyl)thiophene (P3CT, Mw: 30-40k) was purchased from Rieke Metals. All raw materials were directly used without further treatment.

Precursor solution preparations

WBG perovskite precursors: Wide bandgap perovskite precursor solutions (1.2 M, $FA_{0.8}Cs_{0.2}PbI_{1.8}Br_{1.2}$) were prepared with the recipe of 0.96 M FAI + 0.24 M CsI+ 0.48 M PbI_2 + 0.72 M $PbBr_2$ dissolved in 1 mixed solvent DMF/DMSO with volume ratio of 4:1. The precursors were stirred for 1 h to dissolve all chemicals and further filtered with 0.22 μm PTFE membrane before using.

LBG perovskite precursors: Low bandgap perovskite solutions ($Cs_{0.05}FA_{0.7}MA_{0.25}Pb_{0.5}Sn_{0.5}I_3$, 1.8 M) were prepared in the same way as our previous paper.[31] To reduce Sn^{4+} cations in precursor, 5 mg lead was added into the solution with stirred in a glovebox at room temperature for 3 h before use.[19]

HTL and surface passivation solutions: NiOx NPs were distributed decentralized in DI water with a concentration of 10 mg/mL. Me-4PACZ was dissolved in Et-OH (0.3 mg/mL). $PDAI_2$ was dissolved in IPA with a concentration of 1 mg/mL. P3CT and P3CT-Pb were prepared in two steps: the first step is to dissolve 10 mg P3CT or P3CT/PbI_2 (weight ratio of 2:1) in 1 mL DMF and then dilute the high concentration solution with CB into desirable concentration (1 mg/mL for single-junction devices and 3 mg/mL for tandem devices). For pH measurement of P3CT materials, the P3CT powders were dissolved in DMSO (2 mg/mL) and diluted into 0.1 mg/mL with methanol before dipping on pH paper. P3CT-MA and P3CT-Cs were prepared according to the literature.[19] PEIE were diluted with IPA into 0.025 wt%. EDA solutions were prepared via dissolving 1 μL EDA in 20 mL CB. PEDOT:PSS solutions for tandem were prepared by diluting the raw solution with IPA (volume ratio of 1:2).

Devices fabrications:

LBG PSCs: The ITO substrates were ultrasonically cleaned at Micro-90 detergent, H_2O, acetone, and IPA for 20 min, respectively. The ITO substrates were dried under nitrogen flow and further cleaned with UV ozone for 30 min. The PEDOT:PSS HTLs were spin-coated on ITO glass at 4000 rpm for 30 s in ambient conditions and annealed at 140 ˚C for 15 min. While P3CT HTLs were spin-coating in a glovebox (N_2 filled) at 3500 rpm for 30 s, and annealed at 100 ˚C hotplate for 10 min. The PTAA (1 mg/mL in toluene) HTLs were coated on ITO at 4000 rpm for 30 s in glovebox and annealed at 100 °C for 10 min. For good wettability, PFN-Br (0.5 mg/mL in methanol) was coated on PTAA at 6000 rpm for 20 s. The thick MeO-2PACZ (0.5 mg/mL in ethanol) were coated on

ITO at 1500 rpm for 30 s, following annealed at 100 °C for 10 min. After that, 50 μL LBG perovskite precursors were dropped on cooled substrates and spin coating with the procedure of 1000 rpm for 10 s and 3500 rpm for 40 s in the glovebox. The anti-solvent treatment with 400 μL CB was conducted at 20 s before the end of the coating. The wet films were moved to a 100 ˚C hotplate and annealed for 10 min to transmit the intermedium phase into a desirable photovoltaic phase. For surface passivation, 50 μL EDA solution (in CB) was dynamically spin-coated on the cold perovskite films at 5000 rpm for 30 s, and further annealed at 100 ˚C for 5 min. After that, the substrates were transferred to a vacuum chamber to evaporate 25 nm C60, 6 nm BCP, and 130 nm Ag.

All-perovskite tandem devices: The ITO substrates were cleaned with the same procedures as the single-junction devices. NiO_x NPs were then spin-coated on cleaned ITO substrates at 4000 rpm for 30 s without annealing. The substrates were transferred into a glovebox to coat the Me-4PACz HTL at 3000 rpm for 25 s, further annealed at 100 ˚C for 10 min. Then WBG perovskite films were deposited on the substrates at a speed of 3800 rpm for 32 s with an acceleration speed of 1000. 150 μL anisole as antisolvent was fast dropped on the wet films at 22nd s. Annealing at 110 ˚C for 15 min was taken to form high-quality WBG perovskite films. Then $PDAI_2$ was dynamically coated on the cooled WBG perovskite as surface passivation, followed by annealing at 100 ˚C for 5 min. After that, the substrates were transferred into an evaporation chamber to deposit 30 nm C60. Before wettability and growth of atomic layer deposition (ALD), PEIE was spin-coated on the films at 5000 rpm for 30 s without annealing. 25 nm ALD SnO_2 film and 1 nm Au were deposited on the substrates sequentially. Diluted

PEDOT:PSS solution for tandems was spin coated at 3000 rpm for 10 s in the clean room (controlled humidity below 30%) and further dried at 120 ◦C hotplate for 8 min. The P3CT HTLs were coated at 3000 rpm for 30 s in a glovebox and annealed at 100 ◦C for 5 min. LBG perovskite films were coated on the substrates at 800 rpm for 5 s and 3500 rpm for 40 s. 400 μL CB antisolvent was dropped on the films at 20 s before the end of spin procedures. Finally, EDA treatment and C60/BCP evaporation were the same as the single junction devices.

Normal-bandgap PSCs: The normal-bandgap perovskite films were deposited as the same as the literature[52] and we replaced the BCP and Ag with the ALD SnO_2 (15 nm) and Au respectively. Before measurements, the devices were packaged with UV epoxy in a glovebox.

Characteristics

HTLs and perovskite films characteristics: The UV-vis absorption spectra of perovskite films and transmittance spectra of various HTLs were tested on the PerkinElmer Lambda 1050. XPS and UPS spectra of various materials were collected at the Kratos AXIS ULTRA DALD. SEM and XRD measurements were conducted on the Hitachi S-4800 and RigakuUltima III with Cu Kα radiation, respectively. For evaluating the buried morphology and chemical bond environment of perovskite deposited on different HTLs, the LBG perovskite films were peeled off from ITO glass. The processes were to fix the UV epoxy (with cover glass) under UV light and then peel off the perovskite from substrates via fall down several times. To explore the buried perovskite surfaces, the films were firstly aged under 0.9 sun white LED light & 60 ◦C

for several days (glass side toward light and film side on hotplate) and then peeled off for measurements. The AFM and KPFM of various films were collected using a Vecco D500 atomic force microscope. The steady-state photoluminescence (PL) and time-resolved PL (TRPL) measurements were using a custom-built system with Hotiba Symphony-II CCD detector/Horiba iHR 320 and Becke & Hickl TCSPC (HPM100-10, SPM130), respectively. The excited laser was 633 nm for both PL and TRPL measurements. The PLQY of samples was measured by a custom-built system, and the process was the same as the previous report.[31]

SCLC measurements on LBG perovskite films and various HTLs: To estimate the hole mobility of various HTLs materials, the hole-only structure of ITO/NiOx/HTL materials/PTAA/MoO_3/Ag was fabricated. PEDOT:PSS was coated the same as the single junction devices fabrications. The concentration of P3CT-X was increased to 4 mg/mL for thick films (25 nm). The data were collected with Keithly 2400 with the scanning voltage from 0 V to 4 V with 300 scanning points (around 7 min for each scanning). The SCLC measurements of perovskite films were performed based on ITO/HTLs/perovskite/PTAA/MoO_3/Ag. The scanning procedure was 0-1.2 V with 200 scanning points (around 5 min for each scanning).

Time-resolved mass spectroscopy measurements: The TR-MS of each sample were measured on a built-in-house TPD system.[53] The samples were loaded in transparent test tubes with the ITO side toward the light. The samples need to be vacuumed under dark conditions for 12 h to remove the air. The light source was 1 sun Xe lamp (Newport). The data of mass signals were recorded with a step of 10 s.

PSCs characteristics: Both LBG and tandem PSCs were encapsulated with UV epoxy and cover glasses before measurements in ambient conditions. The *J-V* curves were collected using a PV Measurements Inc. solar simulator with AM 1.5G solar irradiation and a Keithley 2400 source meter. The scanning range is -0.1 V to 0.95 V with a rate of 100 mV/s. The area of devices was defined by the overlapping area between the metal electrode (Ag) and ITO, corresponding to 0.073 cm^2. The J_{sc} from J-V curves were confirmed with the external quantum efficiency (EQE) equipment (model IVQE8-C, PV Measurements Inc.). The spectra of the solar simulator and EQE light source were calibrated by the standard silicon solar cells certified by NREL. For tandem PSCs, 530 and 940 lamps were applied to collect the EQE of bottom and top subcells, respectively. The TPC and TPV spectra were conducted on the encapsulated LBG PSCs at a PiCoscope 6454 controlled by a custom-built Python problem. The excited light intensity of 0.8 sun. The EIS and *C-V* spectra of each device were recorded using a Solartron Modulab potentiostat. Thermal stability was tested via aging the LBG devices at 60 ˚C hotplate in a glovebox and measuring the photovoltaic performance regularly.

Stability measurements: The thermal stability of the devices was evaluated by aging the devices (encapsulated) at 60 °C hotplate in a glovebox and collecting the photovoltaic performance in regular time. The MPP stability of single junction and tandem PSCs were tracked under 0.9 sun illumination (white LED) in ambient conditions. A metal mask with an area of 0.0615 cm^2 was covered on devices (glass side) during MPP tracking. The temperature around devices was controlled below 30 ˚C with fan cooling. The MPPT of the normal-bandgap PSCs was conducted by putting the encapsulated

devices into the controlled 60 ˚C oven with the w-LED illuminations. We used the Perturb & Observe (P&O) algorithm to track the performance of our solar cells at the vicinity of the maximum power point (MPP) under continuous light illumination.[54] The MPP tracking data (timestamp, voltage, current, and power) was recorded every ~3.7 s. The algorithm measures the present values of voltage V(k), current I(k), and power P(k). After that, it perturbs the operating voltage $V(k+1) = V(k) \pm \Delta V$ and observes the change of power P(k+1) - P(k). The iteration continues with the voltage perturbation that maximizes the power. The PCE of each device was recorded with a Keithley 2400 source meter.

DFT calculations: The structural relaxation and static self-consistent energy simulations are conducted by the CP2K package at the PBE level.[55, 56] The calculations of formation energies and binding energies are carried out based on a 3-layer $MASn_{0.5}Pb_{0.5}I_3$ perovskite slab model with the typical (001) surface orientation terminated by Sn/Pb-I framework. The computations employed the norm-conserving Goedecker-Teter-Hutter (GTH) pseudopotential alongside a double-ξ valence polarization basis set, obtained through meticulous adjustment of molecular geometries.[57-59] The computations were constrained to the gamma point exclusively, with a consistent energy cut-off threshold of 400 Rydberg retained throughout the analysis. The self-consistent field (SCF) convergence criterion was established at 1×10^{-7} Hartree per atom. Furthermore, Grimme's D3 correction was incorporated to account for intermolecular interactions.[60, 61] The pK_a values of various molecules are calculated with the MarvinSketck software.

The energy barrier associated with the deprotonation-erosion process was calculated for the free state PSS and P3CT molecules before they are absorbed into the perovskite surface, as shown in the equation: $E_f = [E(M^-) + E(HI)] - [E(M) + E(I^-)]$, where $E(M^-)$ denotes the total energy of a deprotonated PSS/P3CT, E(HI) denotes the total energy of a HI molecule, E(M) denotes the total energy of a PSS/P3CT molecule, and $E(I^-)$ denotes the total energy of an I ion.

SUPPLEMENTAL INFORMATION

Supplemental information can be found online at https://dio.org/10.1016/j.joule.2024.XX.XXX.

ACKNOWLEDGMENTS

This material is based upon work supported by the U.S. Department of Energy's Office of Energy Efficiency and Renewable Energy (EERE) under the Solar Energy Technologies Office Award Number DE-EE0008753 and under Hydrogen and Fuel Cell Technologies Office Award Numbers DE-EE0008837 and DE-EE0010740, and by the U.S. Air Force Research Laboratory under agreement number FA9453-19-C-1002. The DFT calculations are performed using computational resources sponsored by the U.S. Department of Energy's Office of Energy Efficiency and Renewable Energy and located at the National Renewable Energy Laboratory, also using resources of the National Energy Research Scientific Computing Center (NERSC), a U.S. Department of Energy Office of Science User Facility located at Lawrence Berkeley National Laboratory, operated under Contract No. DE-AC02-05CH11231 using NERSC award BES-ERCAP0017591. The views expressed in the article do not necessarily represent the views of the DOE or the U.S. Government. The U.S. Government retains and the publisher, by accepting the article for publication, acknowledges that the U.S. Government retains a nonexclusive, paid-up, irrevocable, worldwide license to publish

or reproduce the published form of this work, or allow others to do so, for U.S. Government purposes.

AUTHOR CONTRIBUTIONS

S.F., Z.S. and Y.Y. conceived the idea of this project. N.S. and S.F. fabricated the LBG and WBG solar cells, respectively, and assembled the all-perovskite tandem structure. N.S. prepared all the LBG perovskite samples for various measurements and data collections. Y.X. carried out the DFT calculations and results analyses. L.C. and Y.L. helped to fabricate the LBG PSCs and the samples for SEM measurements of buried bottom surface. X.W. helped with the DFT calculations and results analysis. C.L. and B.C. helped with tandem device optimization and analysis. Y.L. helped to stability measurements and data plots. A.A and R.J.E. measured the PL and TRPL of all samples. Z.H. and D.S.G. collected the KPFM images for different HTLs. K.D. tested the XRD for the samples. P.N.K. and M.J.H helped with PLQY measurements. S.F., N.N., Z.S. and Y.Y. wrote the paper with input from all coauthors. Y.Y. directed this project. All authors discussed the results and reviewed the paper.

DECLARATION OF INTERESTS

The authors declare no competing interests.

REFERENCES

1. Kim, J.Y., Lee, J.W., Jung, H.S., Shin, H., and Park, N.G. (2020). High-Efficiency Perovskite Solar Cells. Chem. Rev. *120*, 7867-7918. 10.1021/acs.chemrev.0c00107.

2. Li, T., He, F., Liang, J., and Qi, Y. (2023). Functional layers in efficient and stable inverted tin-based perovskite solar cells. Joule *7*, 1966-1991. 10.1016/j.joule.2023.08.002.

3. Jiang, Q., Tirawat, R., Kerner, R.A., Gaulding, E.A., Xian, Y., Wang, X., Newkirk, J.M., Yan, Y., Berry, J.J., and Zhu, K. (2023). Towards linking lab and field lifetimes of perovskite solar cells. Nature. 10.1038/s41586-023-06610-7.

4. Rong, Y., Hu, Y., Mei, A., Tan, H., Saidaminov, M.I., Seok, S.I., McGehee, M.D., Sargent, E.H., and Han, H. (2018). Challenges for commercializing perovskite solar cells. Science *361*, eeat8235. 10.1126/science.aat8235.

5. Liu, C., Yang, Y., Chen, H., Xu, J., Liu, A., Bati, A.S.R., Zhu, H., Grater, L., Hadke, S.S., Huang, C., et al. (2023). Bimolecularly passivated interface enables efficient and stable inverted perovskite solar cells. Science *382*, 810-815. 10.1126/science.adk1633.

6. Song, Z., Li, C., Chen, L., and Yan, Y. (2022). Perovskite Solar Cells Go Bifacial-Mutual Benefits for Efficiency and Durability. Adv. Mater. *34*, e2106805. 10.1002/adma.202106805.

7. https://www.nrel.gov/pv/assets/pdfs/best-research-cell-efficiencies.pdf.

8. Zheng, X., Alsalloum, A.Y., Hou, Y., Sargent, E.H., and Bakr, O.M. (2020). All-Perovskite Tandem Solar Cells-A Roadmap to Uniting High Efficiency with High StabilityAll-Perovskite Tandem Solar Cells: A Roadmap to Uniting High Efficiency with High Stability. Acc. Mater. Res. *1*, 63-76. 10.1021/accountsmr.0c00017.

9. De Wolf, S., and Aydin, E. (2023). Tandems have the power. Science *381*, 30-31. 10.1126/science.adi6278.

10. Lin, R., Wang, Y., Lu, Q., Tang, B., Li, J., Gao, H., Gao, Y., Li, H., Ding, C., Wen, J., et al. (2023). All-perovskite tandem solar cells with 3D/3D bilayer perovskite heterojunction. Nature *620*, 994-1000. 10.1038/s41586-023-06278-z.

11. Chen, H., Maxwell, A., Li, C., Teale, S., Chen, B., Zhu, T., Ugur, E., Harrison, G., Grater, L., Wang, J., et al. (2023). Regulating surface potential maximizes voltage in all-perovskite tandems. Nature *613*, 676-681. 10.1038/s41586-022-05541-z.

12. Yang, G., Ni, Z., Yu, Z.J., Larson, B.W., Yu, Z., Chen, B., Alasfour, A., Xiao, X., Luther, J.M., Holman, Z.C., and Huang, J. (2022). Defect engineering in wide-bandgap perovskites for efficient perovskite–silicon tandem solar cells. Nat. Photonics *16*, 588-594. 10.1038/s41566-022-01033-8.

13. He, R., Wang, W., Yi, Z., Lang, F., Chen, C., Luo, J., Zhu, J., Thiesbrummel, J., Shah, S., Wei, K., et al. (2023).Improving interface quality for 1-cm^2 all-perovskite tandem solar cells. Nature *618*, 80-86. 10.1038/s41586-023-05992-y.

14. McMeekin, D.P., Mahesh, S., Noel, N.K., Klug, M.T., Lim, J., Warby, J.H., Ball, J.M., Herz, L.M., Johnston, M.B., and Snaith, H.J. (2019). Solution-Processed All-Perovskite Multi-junction Solar Cells. Joule *3*, 387-401. 10.1016/j.joule.2019.01.007.

15. Lin, R., Xu, J., Wei, M., Wang, Y., Qin, Z., Liu, Z., Wu, J., Xiao, K., Chen, B., Park, S.M., et al. (2022). All-perovskite tandem solar cells with improved grain surface passivation. Nature *603*, 73-78. 10.1038/s41586-021-04372-8.

16. Jiang, Q., Tong, J., Scheidt, R.A., Wang, X., Louks, A.E., Xian, Y., Tirawat, R.,

Palmstrom, A.F., Hautzinger, M.P., Harvey, S.P., et al. (2022). Compositional texture engineering for highly stable wide-bandgap perovskite solar cells. Science *378*, 1295-1300. 10.1126/science.adf0194.

17. Zhou, S., Fu, S., Wang, C., Meng, W., Zhou, J., Zou, Y., Lin, Q., Huang, L., Zhang, W., Zeng, G., et al. (2023). Aspartate all-in-one doping strategy enables efficient all-perovskite tandems. Nature *624*, 69-73. 10.1038/s41586-023-06707-z.

18. Chu, Q.-Q., Sun, Z., Hah, J., Moon, K.-s., Cheng, B., Wang, D., Xiao, P., Zhou, Y., Petrozza, A., Yang, G.-J., et al. (2023). Progress, challenges, and further trends of all perovskites tandem solar cells: A comprehensive review. Materials Today *67*, 399-423. 10.1016/j.mattod.2023.06.002.

19. Zhang, W., Li, X., Fu, S., Zhao, X., Feng, X., and Fang, J. (2021). Lead-lean and MA-free perovskite solar cells with an efficiency over 20%. Joule *5*, 2904-2914. 10.1016/j.joule.2021.09.008.

20. Hu, S., Otsuka, K., Murdey, R., Nakamura, T., Truong, M.A., Yamada, T., Handa, T., Matsuda, K., Nakano, K., Sato, A., et al. (2022). Optimized carrier extraction at interfaces for 23.6% efficient tin–lead perovskite solar cells. Energy Environ. Sci.*15*, 2096-2107. 10.1039/d2ee00288d.

21. Dai, X., Chen, S., Jiao, H., Zhao, L., Wang, K., Ni, Z., Yu, Z., Chen, B., Gao, Y., and Huang, J. (2022). Efficient monolithic all-perovskite tandem solar modules with small cell-to-module derate. Nat. Energy *7*, 923-931. 10.1038/s41560-022-01102-w.

22. Zhang, Z., Liang, J., Wang, J., Zheng, Y., Wu, X., Tian, C., Sun, A., Chen, Z., and Chen, C.C. (2022). Resolving Mixed Intermediate Phases in Methylammonium-Free Sn-Pb Alloyed Perovskites for High-Performance Solar Cells. Nano micro. Lett. *14*, 165. 10.1007/s40820-022-00918-1.

23. Li, C., Song, Z., Chen, C., Xiao, C., Subedi, B., Harvey, S.P., Shrestha, N., Subedi, K.K., Chen, L., Liu, D., et al. (2020). Low-bandgap mixed tin–lead iodide perovskites with reduced methylammonium for simultaneous enhancement of solar cell efficiency and stability. Nat. Energy *5*, 768-776. 10.1038/s41560-020-00692-7.

24. Wang, C., Zhao, Y., Ma, T., An, Y., He, R., Zhu, J., Chen, C., Ren, S., Fu, F., Zhao, D., and Li, X. (2022). A universal close-space annealing strategy towards high-quality perovskite absorbers enabling efficient all-perovskite tandem solar cells. Nat. Energy *7*, 744-753. 10.1038/s41560-022-01076-9.

25. Luo, J., He, R., Lai, H., Chen, C., Zhu, J., Xu, Y., Yao, F., Ma, T., Luo, Y., Yi, Z., et al. (2023). Improved Carrier Management via a Multifunctional Modifier for High-Quality Low-Bandgap Sn-Pb Perovskites and Efficient All-Perovskite Tandem Solar Cells. Adv. Mater. *35*, e2300352. 10.1002/adma.202300352.

26. Lin, R., Xiao, K., Qin, Z., Han, Q., Zhang, C., Wei, M., Saidaminov, M.I., Gao, Y., Xu, J., Xiao, M., et al. (2019). Monolithic all-perovskite tandem solar cells with 24.8% efficiency exploiting comproportionation to suppress Sn(ii) oxidation in precursor ink. Nat. Energy *4*, 864-873. 10.1038/s41560-019-0466-3.

27. Tong, J., Jiang, Q., Ferguson, A.J., Palmstrom, A.F., Wang, X., Hao, J., Dunfield, S.P., Louks, A.E., Harvey, S.P., Li, C., et al. (2022). Carrier control in Sn–Pb perovskites via 2D cation engineering for all-perovskite tandem solar cells with improved efficiency and stability. Nat. Energy *7*, 642-651. 10.1038/s41560-022-01046-1.

28. Zhang, Z., Huang, Y., Jin, J., Jiang, Y., Xu, Y., Zhu, J., and Zhao, D. (2023). Mechanistic Understanding of Oxidation of Tin-based Perovskite Solar Cells and Mitigation Strategies. Angew. Chem. Int. Ed. Engl. *62*, e202308093. 10.1002/anie.202308093.

29. Wang, Y., Lin, R., Wang, X., Liu, C., Ahmed, Y., Huang, Z., Zhang, Z., Li, H., Zhang, M., Gao, Y., et al. (2023). Oxidation-resistant all-perovskite tandem solar cells in substrate configuration. Nat. Commun *14*, 1819. 10.1038/s41467-023-37492-y.

30. Chen, L., Fu, S., Li, Y., Sun, N., Yan, Y., and Song, Z. (2023). On the Durability of Tin-Containing Perovskite Solar Cells. Adv. Sci. e2304811. 10.1002/advs.202304811.

31. Chen, L., Li, C., Xian, Y., Fu, S., Abudulimu, A., Li, D.B., Friedl, J.D., Li, Y., Neupane, S., Tumusange, M.S., et al. (2023). Incorporating Potassium Citrate to Improve the Performance of Tin-Lead Perovskite Solar Cells. Adv. Energy Mater. *13*. 10.1002/aenm.202301218.

32. Zhou, J., Qiu, H., Wen, T., He, Z., Zou, C., Shi, Y., Zhu, L., Chen, C.C., Liu, G., Yang, S., et al. (2023). Acidity Control of Interface for Improving Stability of All-Perovskite Tandem Solar Cells. Adv. Energy Mater. *13*. 10.1002/aenm.202300968.

33. Wu, P., Wen, J., Wang, Y., Liu, Z., Lin, R., Li, H., Luo, H., and Tan, H. (2022). Efficient and Thermally Stable All-Perovskite Tandem Solar Cells Using All-FA Narrow-Bandgap Perovskite and Metal-oxide-based Tunnel Junction. Adv. Energy Mater. *12*. 10.1002/aenm.202202948.

34. Prasanna, R., Leijtens, T., Dunfield, S.P., Raiford, J.A., Wolf, E.J., Swifter, S.A., Werner, J., Eperon, G.E., de Paula, C., Palmstrom, A.F., et al. (2019). Design of low bandgap tin–lead halide perovskite solar cells to achieve thermal, atmospheric and operational stability. Nat. Energy *4*, 939-947. 10.1038/s41560-019-0471-6.

35. Gao, H., Lu, Q., Xiao, K., Han, Q., Lin, R., Liu, Z., Li, H., Li, L., Luo, X., Gao, Y., et al. (2021). Thermally Stable All-Perovskite Tandem Solar Cells Fully

Using Metal Oxide Charge Transport Layers and Tunnel Junction. Solar RRL *5*. 10.1002/solr.202100814.

36. Zhu, J., Luo, Y., He, R., Chen, C., Wang, Y., Luo, J., Yi, Z., Thiesbrummel, J., Wang, C., Lang, F., et al. (2023). A donor–acceptor-type hole-selective contact reducing non-radiative recombination losses in both subcells towards efficient all-perovskite tandems. Nat. Energy *8*, 714-724. 10.1038/s41560-023-01274-z.

37. Chen, B., Yu, Z., Onno, A., Yu, Z., Chen, S., Wang, J., Holman, Z.C., and Huang, J. (2022). Bifacial all-perovskite tandem solar cells. Sci. Adv. *8*, eadd0377. 10.1126/sciadv.add0377.

38. Li, X., Zhang, W., Guo, X., Lu, C., Wei, J., and Fang, J. (2022). Constructing heterojunctions by surface sulfidation for efficient inverted perovskite solar cells. Science *375*, 434-437. 10.1126/science.abl5676.

39. Fu, S., Le, J., Guo, X., Sun, N., Zhang, W., Song, W., and Fang, J. (2022). Polishing the Lead-Poor Surface for Efficient Inverted $CsPbI_3$ Perovskite Solar Cells. Adv Mater *34*, e2205066. 10.1002/adma.202205066.

40. Zhang, W., Yuan, H., Li, X., Guo, X., Lu, C., Liu, A., Yang, H., Xu, L., Shi, X., Fang, Z., et al. (2023). Component Distribution Regulation in Sn-Pb Perovskite Solar Cells through Selective Molecular Interaction. Adv. Mater. *35*, e2303674. 10.1002/adma.202303674.

41. Sun, N., Fu, S., Li, Y., Chen, L., Chung, J., Saeed, M.M., Dolia, K., Rahimi, A., Li, C., Song, Z., and Yan, Y. (2023). Tailoring Crystallization Dynamics of $CsPbI_3$ for Scalable Production of Efficient Inorganic Perovskite Solar Cells. Adv. Funct. Mater. 10.1002/adfm.202309894.

42. Zhang, W., Wang, Y.C., Li, X., Song, C., Wan, L., Usman, K., and Fang, J. (2018). Recent Advance in Solution-Processed Organic Interlayers for High-Performance Planar Perovskite Solar Cells. Adv. Sci. *5*, 1800159. 10.1002/advs.201800159.

43. Li, N., Niu, X., Chen, Q., and Zhou, H. (2020). Towards commercialization: the operational stability of perovskite solar cells. Chem. Soc. Rev. *49*, 8235-8286. 10.1039/d0cs00573h.

44. Li, S., He, B., Xu, J., Lu, H., Jiang, J., Zhu, J., Kan, Z., Zhu, L., and Wu, F. (2020). Highly efficient inverted perovskite solar cells incorporating P3CT-Rb as a hole transport layer to achieve a large open circuit voltage of 1.144 V. Nanoscale *12*, 3686-3691. 10.1039/c9nr08441j.

45. Jiang, Q., Song, Z., Bramante, R.C., Ndione, P.F., Tirawat, R., Berry, J.J., Yan, Y., and Zhu, K. (2023). Highly efficient bifacial single-junction perovskite solar cells. Joule *7*, 1543-1555. 10.1016/j.joule.2023.06.001.

46. Xu, H., Liang, Z., Ye, J., Zhang, Y., Wang, Z., Zhang, H., Wan, C., Xu, G., Zeng, J., Xu, B., et al. (2023). Constructing robust heterointerfaces for carrier viaduct

via interfacial molecular bridges enables efficient and stable inverted perovskite solar cells. Energy Environ. Sci. *16*, 5792-5804. 10.1039/d3ee02591h.

47. Liang, Z., Zhang, Y., Xu, H., Chen, W., Liu, B., Zhang, J., Zhang, H., Wang, Z., Kang, D.H., Zeng, J., et al. (2023). Homogenizing out-of-plane cation composition in perovskite solar cells. Nature *624*, 557-563. 10.1038/s41586-023-06784-0.

48. Zhang, S., Ye, F., Wang, X., Chen, R., Zhang, H., Zhan, L., Jiang, X., Li, Y., Ji, X., Liu, S., et al. (2023). Minimizing buried interfacial defects for efficient inverted perovskite solar cells. Science *380*, 404-409. 10.1126/science.adg3755.

49. Wang, Y.-C., Chang, J., Zhu, L., Li, X., Song, C., and Fang, J. (2018). Electron-Transport-Layer-Assisted Crystallization of Perovskite Films for High-Efficiency Planar Heterojunction Solar Cells. Adv. Funct. Mater. *28*, 1706317. 10.1002/adfm.201706317.

50. Guo, H., Yang, C.Y., Zhang, X., Motta, A., Feng, K., Xia, Y., Shi, Y., Wu, Z., Yang, K., Chen, J., et al. (2021). Transition metal-catalysed molecular n-doping of organic semiconductors. Nature *599*, 67-73. 10.1038/s41586-021-03942-0.

51. Al-Ashouri, A., Kohnen, E., Li, B., Magomedov, A., Hempel, H., Caprioglio, P., Marquez, J.A., Morales Vilches, A.B., Kasparavicius, E., Smith, J.A., et al. (2020). Monolithic perovskite/silicon tandem solar cell with >29% efficiency by enhanced hole extraction. Science *370*, 1300-1309. 10.1126/science.abd4016.

52. Jiang, Q., Tong, J., Xian, Y., Kerner, R.A., Dunfield, S.P., Xiao, C., Scheidt, R.A., Kuciauskas, D., Wang, X., Hautzinger, M.P., et al. (2022). Surface reaction for efficient and stable inverted perovskite solar cells. Nature *611*, 278-283. 10.1038/s41586-022-05268-x

53. Song, Z., Wang, C., Phillips, A.B., Grice, C.R., Zhao, D., Yu, Y., Chen, C., Li, C., Yin, X., Ellingson, R.J., et al. (2018). Probing the origins of photodegradation in organic–inorganic metal halide perovskites with time-resolved mass spectrometry. Sustain. Energ. Fuels *2*, 2460-2467. 10.1039/c8se00358k.

54. Podder, A.K., Roy, N.K., and Pota, H.R. (2019). MPPT methods for solar PV systems: a critical review based on tracking nature. IET Renewable Power Generation *13*, 1615-1632. 10.1049/iet-rpg.2018.5946.

55. Kühne, T.D., Iannuzzi, M., Del Ben, M., Rybkin, V.V., Seewald, P., Stein, F., Laino, T., Khaliullin, R.Z., Schütt, O., Schiffmann, F., et al. (2020). CP2K: An electronic structure and molecular dynamics software package - Quickstep: Efficient and accurate electronic structure calculations. J. Chem. Phys. *152*, 194103. 10.1063/5.0007045.

56. Perdew, J.P., Burke, K., and Ernzerhof, M. (1996). Generalized gradient

approximation made simple. Phys. Rev. Lett. *77*, 3865-3868. 10.1103/PhysRevLett.77.3865.

57. Goedecker, S., Teter, M., and Hutter, J. (1996). Separable dual-space Gaussian pseudopotentials. Phys. Rev. B *54*, 1703-1710. 10.1103/PhysRevB.54.1703.

58. Krack, M. (2005). Pseudopotentials for H to Kr optimized for gradient-corrected exchange-correlation functionals. Theor. Chem. Acc. *114*, 145-152. 10.1007/s00214-005-0655-y.

59. VandeVondele, J., and Hutter, J. (2007). Gaussian basis sets for accurate calculations on molecular systems in gas and condensed phases. J. Chem. Phys. *127*, 114105. 10.1063/1.2770708.

60. Grimme, S., Antony, J., Ehrlich, S., and Krieg, H. (2010). A consistent and accurate ab initio parametrization of density functional dispersion correction (DFT-D) for the 94 elements H-Pu. J. Chem. Phys. *132*, 154104. 10.1063/1.3382344.

61. Grimme, S. (2006). Semiempirical GGA-type density functional constructed with a long-range dispersion correction. J. Comput. Chem. *27*, 1787-1799. 10.1002/jcc.20495.